Determining the Spectral Content of MOSES Images

Jacob D. Parker[1] and Charles C. Kankelborg[2]
[1] NASA Goddard Space Flight Center, USA
[2] Montana State University, USA

Abstract

The Multi-Order Solar Extreme Ultraviolet Spectrograph (MOSES) sounding rocket was launched from White Sands Missile Range on 2006 February 8th, to capture images of the Sun in the He II 303.8 Å emission line. MOSES is a slitless spectrograph that forms images in multiple spectral orders simultaneously using a concave diffraction grating in an effort to measure line profiles over a wide field of view from a single exposure. Early work on MOSES data showed evidence of solar features composed of neither He II 303.8 Å nor the nearby Si XI 303.3 Å spectral lines. We have built a forward model that uses cotemporal EIT images and the Chianti atomic database to fit synthetic images with known spectra to the MOSES data in order to quantify this additional spectral content. Our fit reveals a host of dim lines that alone are insignificant but combined contribute a comparable intensity to MOSES images as Si XI 303.3 Å. In total, lines other than He II 303.8 Å and Si XI 303.3 Å contribute approximately 10% of the total intensity in the MOSES zero order image. This additional content, if not properly accounted for, could significantly impact the analysis of MOSES and similar slitless spectrograph data, especially those using a zero-order (undispersed) image. More broadly, this serves as a reminder that multilayer EUV imagers are sensitive to a host of weak contaminant lines.

Unified Astronomy Thesaurus concepts: Solar transition region (1532); Solar instruments (1499)

1. Introduction

An essential tool used to study remote solar phenomena is the spectrograph. By more closely examining the wavelength of light emitted from the Sun, we gain access to a wealth of information (temperature, density, velocity, etc.) needed to more completely describe the solar plasma and properly inform our models. Slit spectrographs take a very narrow strip of the Sun and disperse the light emitted using a diffraction grating, providing high spectral resolution over a very small spatial field of view. Spectrally resolved images are then built by rastering the slit over a region of interest, requiring a full exposure at every position, which can take on the order of hours to cover a large portion of the solar disk.

An alternative approach is to remove the slit, producing a *slitless* spectrograph. Slitless spectrographs disperse an image over a larger field of view. The data from these instruments, sometimes called overlappograms, have spatial and spectral information overlapped in the dispersive direction. Slitless spectrographs often image in multiple spectral orders, each with a different blend of spatial and spectral information, that can be combined and "inverted" to form a spectrally resolved image of the Sun at every exposure. By doing so, these instruments trade spatial and spectral resolution for much higher cadence.

Slitless spectrographs have been used infrequently for decades to image the Sun, and have recently regained popularity. Only two satellite missions have routinely captured solar slitless spectrograph data: The S082A instrument on *Skylab* (Tousey et al. 1973) and the Res-K instrument of the Russian KRONOS-I mission (Zhitnik et al. 1998). These two instruments have informed the recent development and proposal of another full disk slitless spectrograph, the COronal Spectroscopic Imager in the EUV (COSIE; Winebarger et al. 2019; Golub et al. 2020). The currently operating Extreme-ultraviolet Imaging Spectrograph (EIS; Culhane et al. 2007) on the Hinode mission (Kosugi et al. 2007) includes 40″ and 266″ slots that can produce an overlappogram that has been used in a limited number of quantitative studies (Harra et al. 2017, 2020). In addition to these satellite missions, several sounding-rocket-based slitless spectrographs have recently imaged the Sun, including The Multi-Order Solar Extreme ultraviolet Spectrograph (MOSES; Fox 2011), the Extreme ultraviolet Snapshot Imaging Spectrograph (ESIS; J. D. Parker et al. 2022, in preparation; R. T. Smart et al. 2022, in preparation), and the recently launched Marshall Grating Incident X-ray Spectrometer (MaGIXS; Athiray et al. 2019) that was flown with a 12′ × 33′ slot.

MOSES was launched for the first time from White Sands Missile Range on 2006 February 8th. The primary science goal of MOSES was to measure line profiles in He II 303.8 Å over a wide field of view ($\approx 20' \times 10'$) at every exposure. By imaging simultaneously in multiple orders, $m = -1$, 0, and 1, MOSES captures three different projections through a spatial-spectral cube, $I(x, y, \lambda)$, that can be combined and inverted to return a line profile at every pixel over its large field of view, at every exposure. Various inversion methods have been used to return line profiles thus far, mostly for small explosive events in He II 303.8 Å (Fox et al. 2010; Fox 2011; Courrier & Kankelborg 2018; Rust & Kankelborg 2019).

Early work with MOSES images revealed faint solar features when subtracting different spectral orders, as well as in the residuals while inverting, that could not be attributed to He II 303.8 Å. These features could not be attributed to the most obvious sources of spectral contamination, including the nearby Si XI 303.3 Å, or two bright iron lines, Fe XV 284 Å and Fe XVI 335 Å. The periodic multilayer coatings used on the MOSES primary and secondary optics were designed to allow

for optimal throughput at 304 Å but to suppress the close iron lines, Fe XV 284 Å and Fe XVI 335 Å, as much as possible (Owens et al. 2005) making them an unlikely source of contamination. Moreover, if much of the contamination were attributable to one of these strong lines, then the contaminant features should appear twice in the difference images: once at the correct location on the Sun, and again in inverted intensity at a predictable offset. However, such a pattern was not observed (Fox 2011). Si XI 303.3 Å, which is too close in wavelength to be removed by the MOSES multilayer coating, was always expected to be a contamination source in the data. With a spectral dispersion of $\approx$29 mÅ per pixel ($\approx$30 km s^{-1} per pixel), features in Si XI 303.3 Å are dispersed roughly 15.7 pixels from He II 303.8 Å and therefore are easily distinguishable features in He II 303.8 Å. Therefore, these unexpected solar features must be from emission at dimmer and less obvious wavelengths in the MOSES passband. In this paper, we identify and quantify the sources of spectral contamination in the MOSES images. We also comment on the MOSES design decisions that led to this confusion, and how similar instruments can be adapted to better control spectral contamination.

In Section 2, we present a time-averaged set of images from the 2006 MOSES flight, as well as four cotemporal and coaligned images from SOHO EIT. We also discuss the unexpected solar features of unknown spectral content found in the MOSES data. Section 3 describes our methods for identifying and quantifying sources of spectral contamination. This includes using the cross-correlation of MOSES difference images as an indication of significant spectral contamination (Sections 3.1 and 3.2) and how we combine data from EIT with synthetic spectra from the Chianti database (Dere et al. 1997; Del Zanna & Young 2020) to generate synthetic MOSES images that can be fit to MOSES images (Section 3.3). Section 4 shows our best fit to the MOSES data, the resulting spectral content of the time-averaged MOSES images. We discuss our results and their implications for future missions of this kind in Section 5.

2. Data

2.1. MOSES

The MOSES sounding rocket launched from White Sands Missile Range on 2006 February 8th at 18:44 UT. It recorded 27 exposures between 18:44:17 and 18:49:13 UT above $\sim$160 km in altitude, an altitude that roughly corresponds to 50% atmospheric transmission for 304 Å radiation. Exposure times ranged from .25-24 seconds with a roughly 6 second readout time in between. An exposure consists of three images taken simultaneously, one for each of the three spectral orders $m = -1$, 0, and 1. Each MOSES image is 2048 by 1024 pixels with a spatial plate scale of $[x, y] = [0.6, 0.6]''$ pix^{-1}. The $m = 1$ and -1 orders have a spectral dispersion of $\approx$29 mÅ per pixel. For the rest of the paper, we will refer to the mth-order MOSES image as I_m. All data were dark-subtracted and coaligned to exposure number 13 prior to our study (Fox et al. 2010).

To increase signal to noise, we form a single time-averaged image in each spectral order. The wide range of exposure times obtained during the flight guarantees that well-exposed, unsaturated intensities are available at every spatial location. Saturated pixels are replaced with IEEE NaN (Not a Number)

and treated as missing data. Since MOSES observes through a time-varying column of atmosphere throughout its flight, the signal as a function of time varies throughout the flight, exposure time (making the amount of time the shutter is open) an unreliable measurement of expected signal in each image. Therefore, we chose to use median of each image as a proxy, or substitute, for exposure time, when forming our time-averaged image. At each spatial pixel, in each spectral order, the average intensity is the sum over time of unsaturated intensities divided by the sum of their proxy exposure times. This procedure also renormalizes the three MOSES spectral orders to the same sensitivity. The top row of Figure 1 shows the time-averaged versions of I_1 and I_0.

Identifying solar features in the MOSES data that originate at wavelengths different from He II 303.8 Å is simple. Subtracting I_0 (which contains no spectral dispersion) from either outboard order (I_{+1} or I_{-1}) eliminates stationary 303.8 Å features. What remains are bipolar features of various spatial scales along the dispersion direction, which is horizontal. A feature in the principle spectral line, He II 303.8 Å, with a nonzero line-of-sight (LOS) velocity is translated along image rows. MOSES has a spectral dispersion of $\approx$30 km s^{-1} per pixel, leading to a shift of less than 10 pixels for even the fastest LOS velocities in He II. This results in a bipolar feature with obvious positive and negative counterparts that are immediately next to one another. Events like these have been studied in detail by several authors (Fox 2011; Courrier & Kankelborg 2018; Rust & Kankelborg 2019).

Features from other emission lines in the MOSES passband have shifts greater than 10 pixels and cannot be mistaken as Doppler shifted features in He II 303.8 Å. A feature in Si XI 303.3 Å, the next closest line, would be shifted by 15.7 pixels. Si XI features can be seen just above the solar limb, where He II has little to no contribution. The best example of this is region 3, boxed in red in Figure 1. Box 1 of Figure 1(c) has a large, coherent, negative feature dubbed the "wishbone." The wishbone's smooth, large-scale morphology suggests a coronal feature and has no obvious positive counterpart. Close inspection reveals a light smear to its left that is likely a shifted wishbone in the plus order. Unfortunately, the positive portion of the wishbone is too blurry to quantify its shift by inspection. A previous study of these features by Rust (2017) used a wavelet transform to isolate large-scale features prior to taking the difference. That procedure allowed Rust (2017) to roughly identify a contribution from Mg VIII 315 Å to regions 1 and 2. Rust (2017) also identified a faint copy of the limb, $\approx$200$''$ to the right of region 3 that was attributed to Si IX/ Fe VI 296.1 Å. Although the probable sources of contamination were identified, their contributions to the total image intensity were not quantified.

2.2. EIT

The Extreme ultraviolet Imaging Telescope (EIT; Delabou*dinière et al. 1995) on board the Solar and Heliospheric Observatory (SOHO) captured four full-disk EUV images, one in each of the 171, 195, 284, and 304 Å channels (Figure 2) within $\approx$20 minutes of the 2008 MOSES flight. Prior to use, each image was first despiked using `iris_prep_despike. pro` with default settings and made level 1 with `eit_prep. pro`. They were then rotated to 2006 February 08 18:47 UT, the time stamp of image 13 of the MOSES observing sequence (Fox 2011), using `drot_map.pro`. EIT and MOSES were
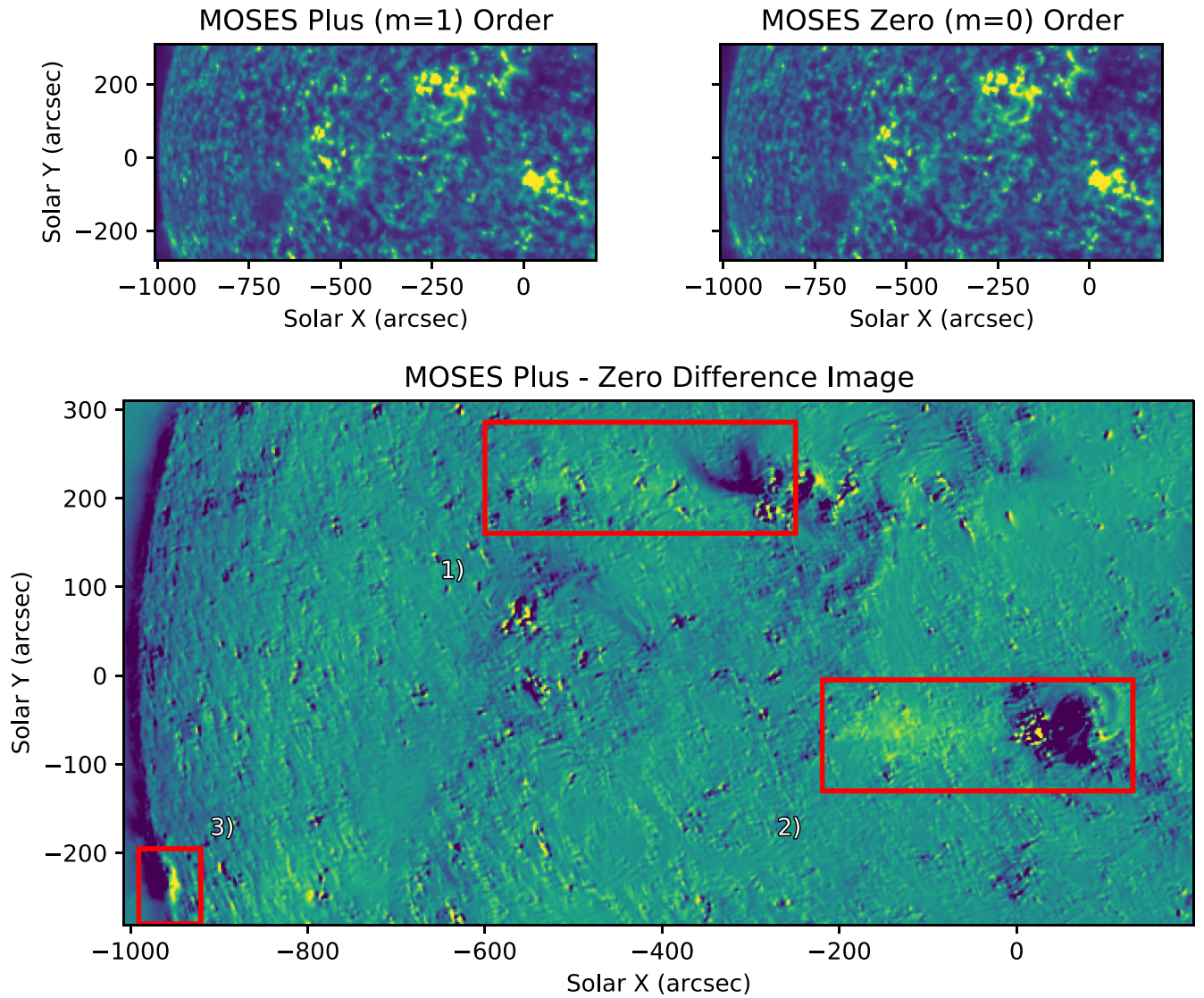
Figure 1. Time-averaged images for the $m = 0$ and 1 spectral orders (top row), followed by their difference, $m = 1$ minus $m = 0$. Regions one through three, boxed in red, show regions of high spectral contamination. Dark features from the $m = 0$ order are adjacent to yellow smears with pixel shifts too large to be Doppler shifts.

coaligned by applying the affine coordinate transform to EIT 304 Å that maximized the zero-lag cross-correlation between it and the time-averaged $m = 0$ order image described in the proceeding subsection. The same transform was then applied to the other three EIT channels.

At first glance, one can find all features boxed in the MOSES difference images (Figure 1) in the EIT 171, 195, and 284 images (Figure 2). The wishbone (box 1) is clearly visible in 171 and 284, the small active regions (box 2) in 171, 195, and 284, and the bright feature at the limb (box 3) is seen most clearly in 195 and 284. The presence of these features in MOSES data indicates a contribution of coronal spectral lines to an otherwise transition region image. While similarities between MOSES difference images and EIT images indicate the contribution of hotter lines to MOSES He II data, they do not straightforwardly tell how much or by which lines. In Section 3, we set out to quantify the intensity contributed by each source of spectral contamination in the MOSES image.

3. Methods

3.1. Difference Image Cross-correlation

To help identify signatures of hot spectral lines, we cross-correlated the MOSES difference images along the dispersion direction, or image rows. Performing a cross-correlation on the difference images requires justification. An obvious first choice would have been to simply cross-correlate I_0 with either outboard order. Unfortunately, the correlation function is dominated by the autocorrelation of the He II signal, as seen in Figures 3(d) and (e). These example cross-correlations show two main peaks in correlation that are due to the autocorrelation of bright He II features, and not spectral contamination. This would also be the case when cross-correlating I_{+1} and I_{-1}. By taking the difference, we remove stationary He II objects (Figures 4(d) and (e)), and in turn, their autocorrelation from the cross-correlation function (Figure 4(f)), leaving only peaks in correlation from features not of He II 303.8 Å.
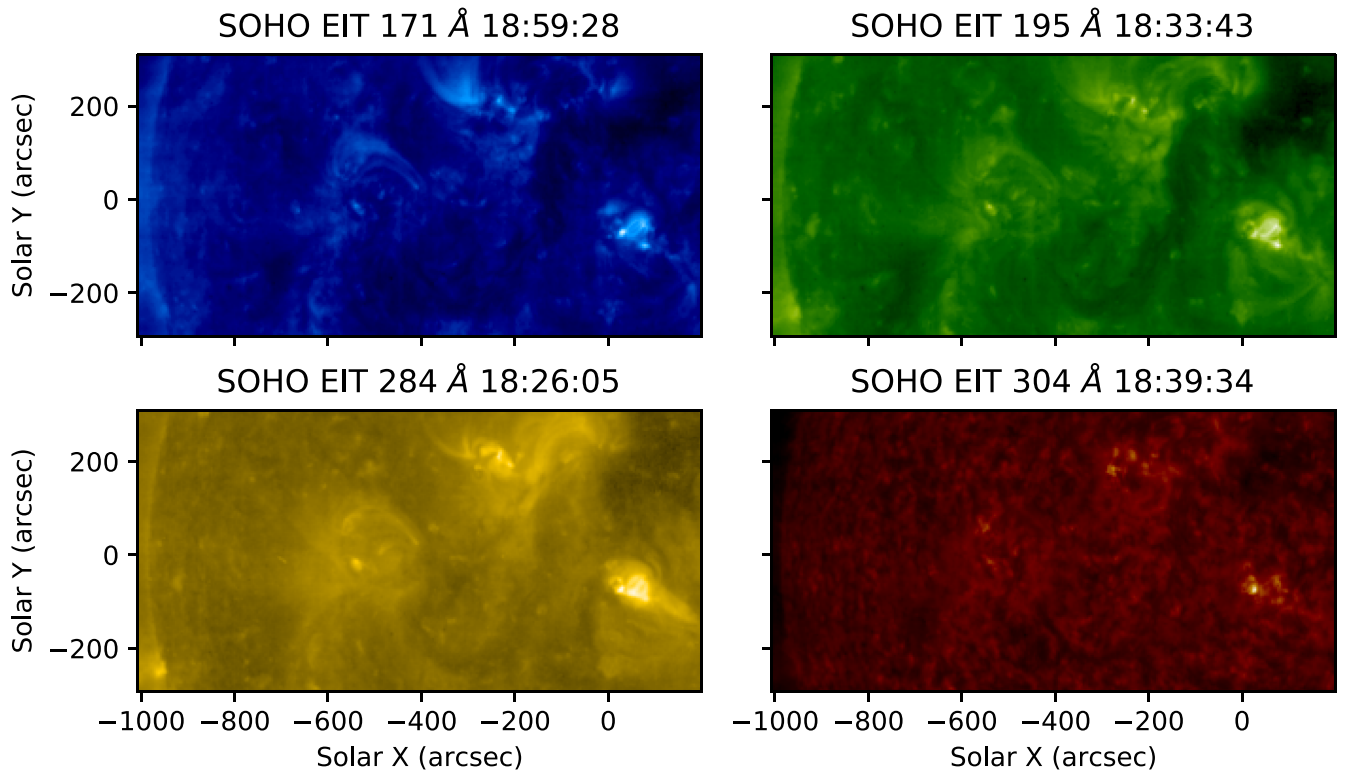
Figure 2. SOHO EIT Images taken closest the MOSES Launch on 2006 February 8th. Each image was rotated to 2006 February 08 18:47 UT to match the middle MOSES exposure time. After rotation, the EIT 304 channel was linearly coaligned to the MOSES zero order, and then the same transformation was applied to every other channel. Each image has been fourth root scaled.

The cross-correlation of two difference images along their rows is defined to be

$$(I_{+1} - I_0) \otimes (I_{-1} - I_0) = \mathcal{F}_x^{-1}\{\mathcal{F}_x(I_{+1} - I_0)\mathcal{F}_x(I_{-1} - I_0)^*\},$$
(1)

where $\mathcal{F}_x$ is the Fast Fourier Transform (FFT) operator applied along image rows. Also, image rows were padded with zeros prior to applying the FFT, to minimize effects of wraparound. Notice that edge effects are practically absent because of our choice to work with image differences. Consequently, windowing was not necessary. This yields a one-dimensional cross-correlation function for each row of the MOSES difference images. Since we are concerned mostly with bulk spectral content, we then take the mean of all 1024 cross-correlation functions, one for each row, to get our final correlation curve plotted in red in Figure 5.

The mean cross-correlation curve for the MOSES difference image has a few notable features. There are large peaks in correlation at approximately -1800, -500, 250, 800, and 1500 pixel lags. The largest peak in correlation is centered about zero lag and is quite broad. While these features are identifiable, the curve is complicated enough that attributing a given peak to particular spectral content is difficult and the significance of any given peak is questionable. We therefore move to test the null hypothesis that none of these features are due to spectral contamination and that they are instead the result of random fluctuations in the data. We explore this null hypothesis in the Section 3.2 by cross-correlating random data generated to emulate the scales present realistic solar features, such as those found in the MOSES image rows. Once we have demonstrated that the peaks in correlation are significant, we will use a

forward model to generate synthetic MOSES images, with known spectral content, that can be cross-correlated and compared to the real MOSES images. Section 3.3 outlines this process, and Section 4 discusses the results.

3.2. Significance Testing

The mean cross-correlation function of the two MOSES difference images, red in Figure 5, has several interesting peaks in correlation. As can be seen in Figure 4(e), these peaks can be indicative of extra spectral content. Actual MOSES images contain information not represented in the Figure 4 cartoon. Each MOSES order has a slightly different point-spread function, and the He II features are not all stationary. This leads to many extra small-scale features in the difference images across the field of view. It is also unclear what magnitude of cross-correlation we should expect from extra spectral content. We therefore move to test the null hypothesis that the features in the MOSES difference image cross-correlation curve are the result of random correlations between each difference image and are not indicative of extra spectral content.

To investigate the null hypothesis, we require test solar data that match the MOSES image rows in length and have similar power spectra and autocorrelation. MOSES images contain 2048 columns. These columns have the same spatial features as MOSES image rows and the same noise distribution, but with none of the repeating patterns that arise from contaminant spectral lines. Therefore, MOSES image columns fairly represent how the MOSES image rows would appear under the null hypothesis. Despite this, the MOSES image columns are insufficient for significance testing, in two ways. First, there is an insufficient sample size. Since most solar features in a MOSES image are larger than a pixel, adjacent columns can have similar
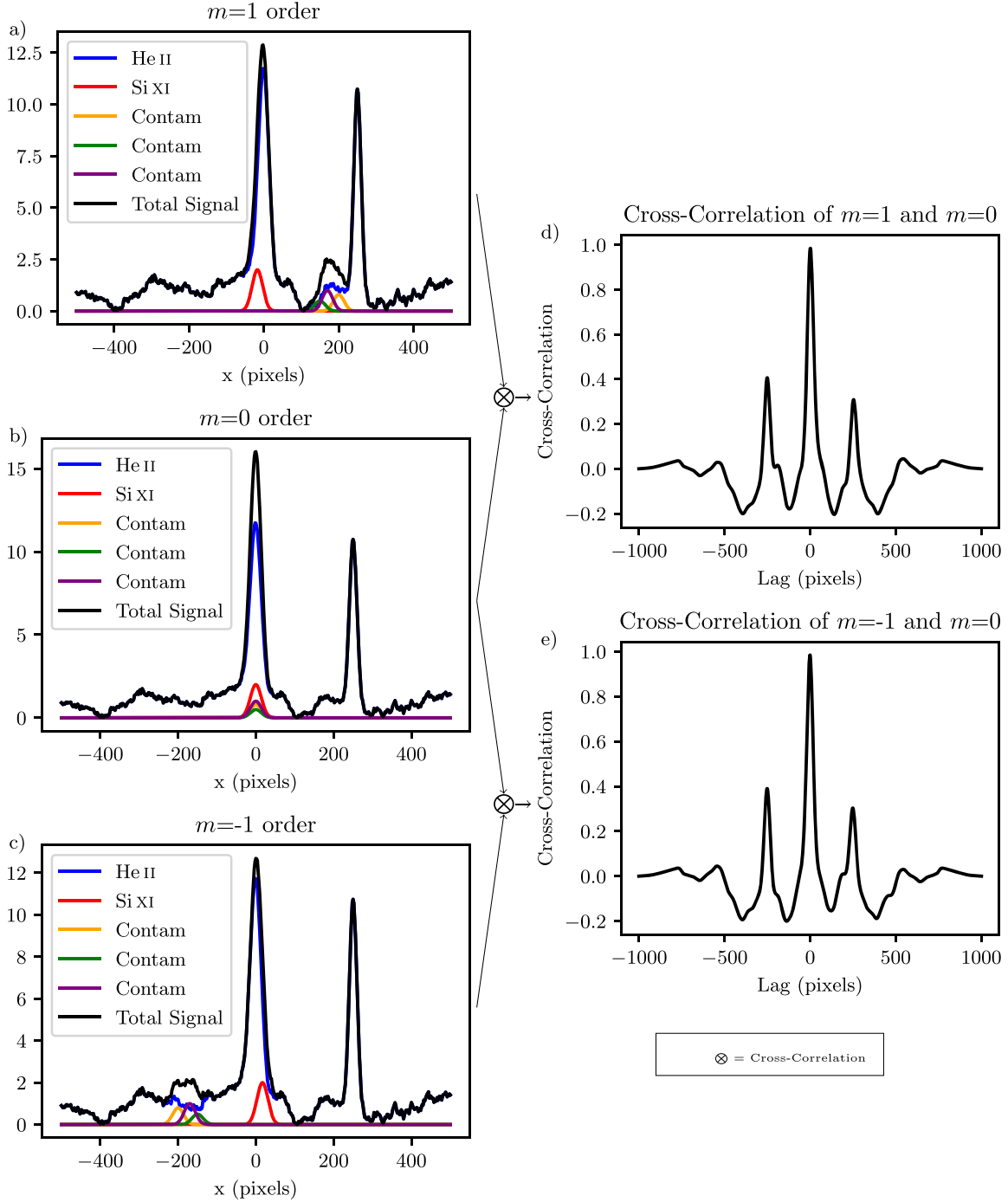
Figure 3. A cartoon example of a 1D MOSES row in the $m = 1$ (a), 0 (b), and -1 (c) spectral orders followed by the cross correlation of $m = 1$ and 0 (d) and the cross-correlation of $m = -1$ and 0 (e). The cross-correlation of any two MOSES orders is dominated by the autocorrelation of stationary He II features and background, making it difficult to identify the additional spectral content. The strong peaks in correlation at ± 250 pixels are the result of the two bright He II features at 0 and 250 overlapping.

cross-correlations and are therefore are not statistically independent measures of spectral content (or lack thereof). Solar features in the MOSES images range from ≈ 4–100 pixels in size. Therefore, we can expect to have at most $2048/4 = 512$ and as few as $2048/100 \approx 25$ independent columns. Second, MOSES columns are half as long as the rows, preventing us from measuring the significance of correlation past 1024 pixel lag. Therefore, we require additional steps to generate a test data set for significance testing.

Using the MOSES image columns as our basis, we generated N random arrays that are 2048 pixels long and resemble MOSES columns in structure. First, each time-averaged MOSES image, I_{mxy}, is windowed with a Hanning window, w_y, and Fourier transformed along the column dimension, y. The windowed Fourier transformed array is defined to be

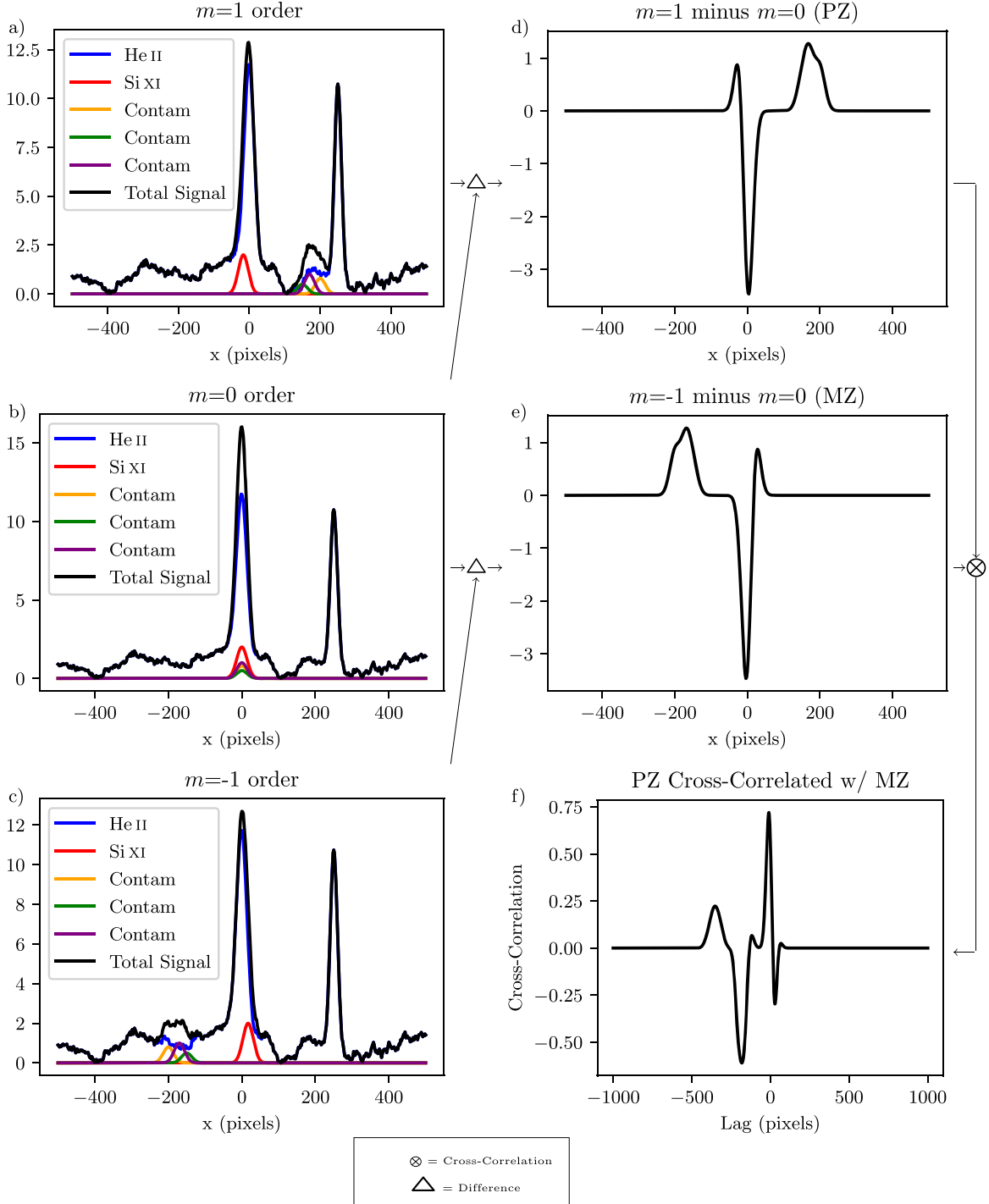$$\tilde{I}_{mxk_y} = \mathcal{F}_y[w_y I_{mxy}]. \tag{2}$$

Figure 4. The same cartoon rows from Figure 3 are shown. Two possible differences between them, $m = 1$ minus $m = 0$ (d) and $m = -1$ minus $m = 0$ (e), are cross-correlated (f). Taking a difference removes stationary He II features, so that peaks in cross-correlation are only from the extra spectral content. Even in this simple 1D example, assigning each peak to a contributing spectral line is difficult. This demonstrates the need for a forward model to interpret the average cross-correlation curve from the MOSES data.

The spatial dimensions x and y represent MOSES image with $x = 0, 1, \ldots, 2047$ and $y = 0, 1, \ldots, 1023$.

From the set of all the Fourier transformed data columns, we will generate a test *row* for each order, I'_{mx}, by populating its Fourier transform, $\tilde{I}'_{mk}$. Each new array is formed by picking an element randomly from the distribution of Fourier transformed columns. Importantly, the same random choice is used for each spectral order, m. The transformation outlined in Equation (2)

gives a distribution of 511 spatial frequency bins and one DC bin that each have 1024 elements (one from each column) for each order. Once assembled, each array is further scrambled by giving each value of k, aside from the DC term, a random phase shift, $e^{i\phi}$, with $\phi \in (0, 2\pi]$ drawn from a uniform distribution. The same random phase ϕ is employed for the kth Fourier component of each spectral order, producing three simulated rows that differ only according to the spectral order from which

Mean Cross-Correlation Distribution using 1024 Rows

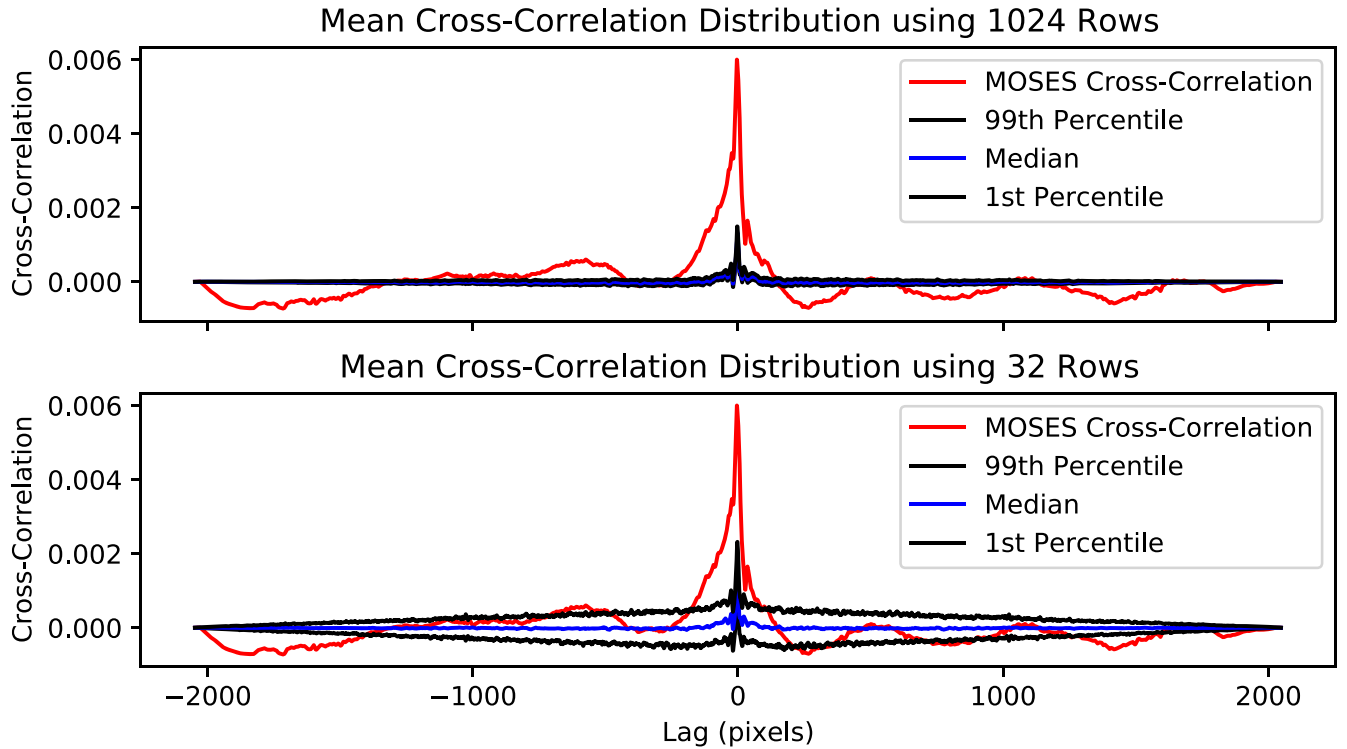## Mean Cross-Correlation Distribution using 32 Rows

Figure 5. The mean cross-correlation function of MOSES difference image rows (red) is compared to a distribution of mean cross-correlations from a selection of randomly generated test row differences (Section 3.2). The top panel shows the distribution after taking the mean of 1024 (the number of MOSES rows) randomly chosen test row differences 10,000 times. The bottom panel challenges that all 1024 rows of MOSES are unique and shows the distribution for only 128 randomly chosen difference rows, also 10,000 times. In either case, the mean cross-correlation values from the MOSES data exceed the 98% confidence interval and are therefore deemed significant and indicative of spectral content in the MOSES data.

they were taken. In order to create an array that is 2048 elements long from one that is 1024 elements long, we require twice as many values of k as k_y:

$$k_y = \begin{cases} 0, & k = 0, \\ \mathtt{ceil}\left(\frac{k}{2}\right), & 0 < k < 1023, \\ 511, & k = 1023, \\ 512, & k = 1024, \end{cases} \quad (3)$$

where ceil rounds up to the nearest integer, and the k-indices are arranged as they traditionally are in the fast Fourier transform. Since our data are purely real, we can fill in the remaining Fourier components, negative frequencies, with the complex conjugate of the corresponding positive frequency component. Finally, all synthetic rows of spectral order m are found through an inverse FFT,

$$I'_{mxn} = \mathcal{F}_x^{-1}[\tilde{I}'_{mkn}]. \quad (4)$$

We examined randomly drawn 1024-pixel segments from the 2048-pixel synthetic MOSES test rows and compared their power spectra to those of the original columns. The 10th percentile, median, and 90th percentile power spectra of both sets match extremely well, giving us confidence that our wavenumber interpolation scheme was properly implemented and yielded plausible distributions of intensity in the test rows.

Now that we have created a set of 10,000 test rows for each order m, we can cross-correlate the order-difference for each row, as we did for MOSES. This yields a set of 10,000 test difference row cross-correlation functions. Since we are interested in the average MOSES difference row

cross-correlation, we choose a number of test row cross-correlations and average them together before comparison. The blue and black curves in the top panel of Figure 5 show the results of picking 1024 random test cross-correlations (the same number of rows as a MOSES image) and taking their average. We do this 10,000 times and form a distribution of mean cross-correlation values at each pixel lag. The 1st and 99th percentile of the distribution are plotted in black, and the median in blue. From the top panel of Figure 5, it is clear that a mean cross-correlation much greater or less than zero is highly unlikely in our test rows with no spectral content. The exception to this is at zero lag when a positive peak in correlation well above zero is typical. Despite this exception, the peak in mean cross-correlation from the MOSES data is much greater, and broader, than that of the test data. The comparison in the top panel of Figure 5 assumes that all 1024 difference rows from the MOSES data are unique. Since solar features in the MOSES images exceed a single pixel in size, this is unlikely. The bottom panel of Figure 5 is made in the same way as the top panel, but uses the mean of only 32 rows when forming the distribution. We believe 32 independent rows represents a reasonable lower bound, after examining the autocorrelation length of the MOSES rows and seeing a large falloff in autocorrelation ($\approx$75% on average) by 32 pixel lag. Even when we assume that MOSES has only 32 unique rows, we can see the same five large peaks in the MOSES mean cross-correlation (identified in Section 3.1) fall outside the 98% two-sided confidence interval.

From this study, we find that the shape and magnitude of the largest peaks in the mean cross-correlation of the MOSES

difference images are significant and indicative of spectral content. We therefore wish to quantify that spectral content.

3.3. Forward Model

In this section, we use a forward model of the MOSES instrument to form synthetic images with a known spectral content and fit them to the MOSES data in order to identify and quantify the sources of spectral contamination. In particular, we wish to reproduce the broad undulations that are present in the MOSES cross-correlations in Figure 5, which were shown in the previous section to be statistically significant. In order to interpret how these peaks in correlation relate to spectral content of the MOSES images, we developed a forward model that produces synthetic MOSES difference images with known spectral content using the four cotemporal EIT images and Chianti. Each of the four images from EIT are used with a Solarsoft DEM tool to produce a DEM cube, a solar image at each temperature from $\log T = 4$–6.5 K in increments of $\log T = .1$K (Cook et al. 1999). We then normalize that DEM cube by the average DEM of the cube predicted by the DEM tool, so that each temperature image has an average emission measure of unity over the MOSES field of view, leaving only the spatial distribution of intensity at each temperature. From this normalized DEM cube, we can produce synthetic MOSES data with different spectral content by assigning an average DEM of our choosing to the cube (multiplying each spatial pixel by the same DEM) prior to folding it through the MOSES instrument forward model. These synthetic images can be cross-correlated in the same way and compared to the mean MOSES cross-correlation function. We can then modify the average DEM assigned to the DEM cube until the synthetic data best fits the MOSES data. More details on the creation of the synthetic MOSES images for each order m, I'_{mxy}, are described in the following procedure.

1. Form a map of differential emission measure (DEM), ξ_{xyT}, a DEM at every spatial pixel, from four cotemporal and coaligned EIT images.
2. Normalize ξ_{xyT} to have an average emission measure of unity over the MOSES field of view at every temperature.
3. Calculate the contribution function, $G_{\lambda T}$, over the range $\log T = 4$–6.5 K for each spectral line between 280 and 340 Å using a unit emission measure.
4. Form a synthetic line image at each temperature for every spectral line:

$$I'_{xy\lambda T} = \xi_{xyT} G_{\lambda T} \qquad (5)$$

5. Shift $I'_{xy\lambda T}$ along image rows according to the MOSES spectral dispersion δ. Sum the dispersed map multiplied by the MOSES optical throughput, $\alpha_{m\lambda}$, along the wavelength axis:

$$I'_{mxyT} = \sum_{\lambda} I'_{\left(x-m\frac{\lambda-303.78}{\delta}\right)y\lambda T} \alpha_{m\lambda}. \qquad (6)$$

6. Multiply by desired spatially averaged DEM and integrate in temperature to form a synthetic MOSES image in each order:

$$I'_{mxy} = \sum_{T} I'_{mxyT} \, \text{DEM}_T \, dT. \qquad (7)$$

We calculate the DEM map, ξ_{xyT}, using the `eit_dem_tool.pro` tool provided in Solarsoft, which combines the four prepped EIT images described in Section 2.2 and gives a DEM for each pixel across the full EIT field of view (Cook et al. 1999). This DEM tool uses the Chianti active region DEM to form synthetic spectra that can be combined with EIT instrument response to get the expected EIT intensity in every channel. The DEM can then be modified for each pixel until it best matches the data.[3] To coalign ξ_{xyT} to MOSES, we apply the same transformation to each temperature image in the map that we applied to the EIT 304 Å channel when coaligning to the MOSES zero-order image. We normalize the DEM map by its spatial average at each temperature over the MOSES field of view. We do this because we are more concerned with the spatial distribution of intensity at a given temperature than the absolute DEM predicted by the code. Also, starting with a normalized DEM map allows us to use the average emission measure over the field of view at each temperature as the free parameters in our fit.

In order to create a synthetic MOSES image at each spectral order, we must combine ξ_{xyT} with spectral information. Using the Chianti database, we generate a synthetic line list using a constant log pressure of $15 \, \text{K cm}^{-3}$, Feldman coronal abundance (Feldman 1992), and a flat log DEM, $\log \text{DEM}(T) = 1 \, \text{cm}^{-5} \, \text{K}^{-1}$. Since MOSES images spectral lines formed over a large range of temperatures, choosing a constant density when creating synthetic spectra would poorly represent data. We therefore choose to use a constant pressure that gives a log density of $9 \, \text{cm}^{-3}$ at 1 MK and increases by an order of magnitude in density for each order of magnitude decrease in temperature. Leaving the line list unsummed in temperature gives the intensity as a function of temperature for each spectral line in the passband, $G_{\lambda T}$. Combining $G_{\lambda T}$ with ξ_{xyT} and the wavelength-dependent MOSES throughput, $\alpha_{m\lambda}$, yields an image for every spectral line at every temperature, $I'_{xy\lambda T}$. The MOSES throughput is defined by the periodic metallic multilayer coatings on the MOSES primary and secondary optics, as well as the thin-film aluminum filters just before the detector.

The MOSES grating has a spectral dispersion of $\delta = \approx 29$ mÅ per pixel. Therefore, in order to produce a set of images for each of the three MOSES spectral orders, $m = -1, 0, 1$, line images, $I'_{xy\lambda T}$, must be shifted along x. Each image is shifted by n pixels, where $n = m\frac{\lambda - 303.78}{\delta}$. This results in no shift for the central $m = 0$ order, and an equal and opposite shift in the outboard orders, $m = -1$ and 1. When shifting line images to form the outboard orders, we allow features outside the field of view defined by the MOSES zero order to shift into the field of view, which is possible because each EIT image is full-disk. This mimics the behavior of the actual MOSES optical system because MOSES does not have a stop to strictly enforce its FOV, thus making it is possible for highly shifted features to exist in the outboard orders that are not captured by the ESIS zero order and vice versa. After the line image at each temperature is shifted, we sum each order in wavelength to form an image in each order at every temperature bin, I'_{mxyT}.

Final synthetic MOSES images are formed at each order by multiplying I'_{mxyT} by an average DEM of choice and integrating in temperature (Equation (7)). This gives three synthetic MOSES images from which we can form difference images and cross-correlate (Equation (1)). Using each temperature bin

---

[3] Detailed description found in `user_guide.pdf`, distributed with the SOHO EIT package in SSW.
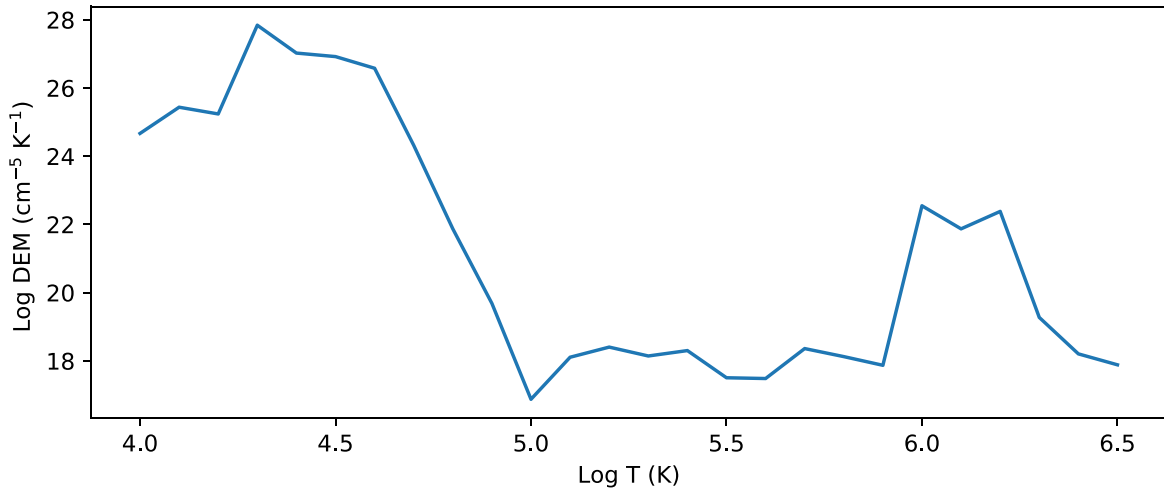
Figure 6. Our forward model uses the average DEM of the synthetic data as the free parameter when fitting MOSES data. The average DEM of best fit is shown here.
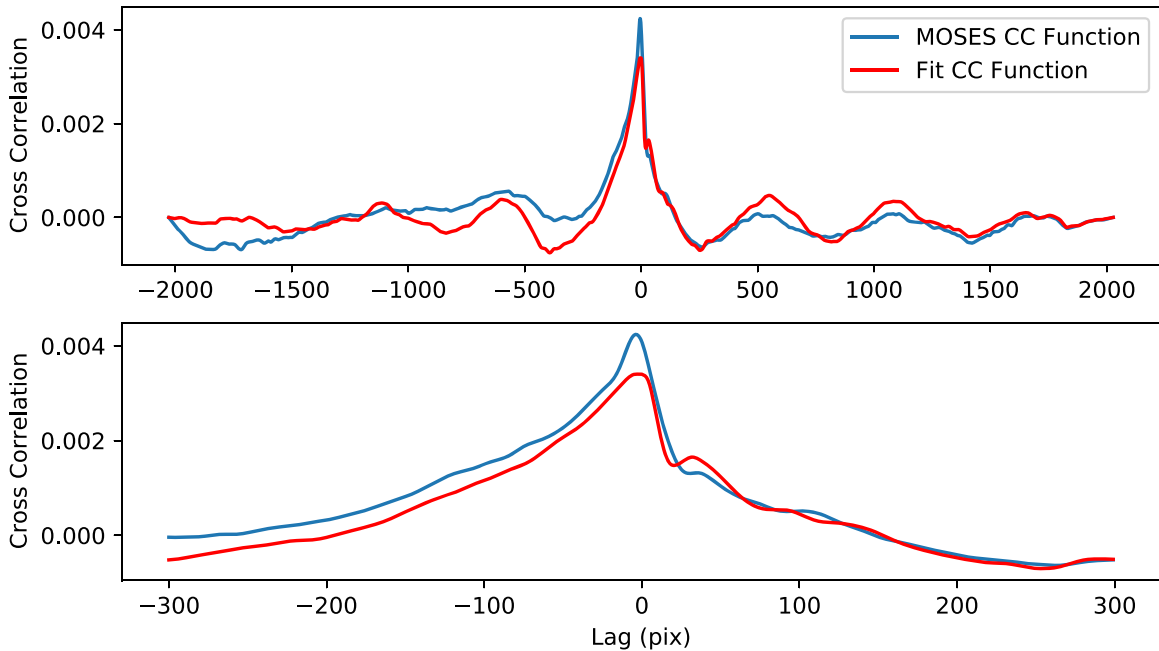

Figure 7. The top panel shows the entire mean cross-correlation along image rows of the MOSES (blue) and best-fit synthetic (red) difference images. The bottom panel shows a zoomed-in view of the same function in order to highlight features near zero lag.

of the chosen average DEM as a free parameter, we seek to minimize the least-squares difference between the synthetic and MOSES mean cross-correlation functions, yielding closely matching synthetic MOSES data with known spectral content.

When comparing our synthetic data to MOSES, we slightly blur each MOSES image prior to taking the difference and cross-correlating using a normalized Gaussian kernel with a standard deviation of four pixels. This ensures that small-scale features (which are not indicative of spectral contamination) in the MOSES images do not impact the fit. During testing, it was found that the width of the kernel used had little impact on the final results (a few percent difference in final spectral content), therefore a standard deviation of four pixels was chosen based on the factor of ≈ 4 difference in resolution between EIT and MOSES and a visual comparison of small-scale features in the resulting, blurred, difference images.

In the following section, we show the DEM of best fit to the MOSES data, as well as the resulting synthetic difference images and total spectral content.

4. Results

Using the forward model described in the previous section, we have generated synthetic MOSES images with a known spectral content that best fit the MOSES data. We achieved a best fit by varying the emission measure at each temperature prior to integrating and then comparing the cross-correlation of the synthetic difference images to that of the MOSES difference images. The DEM of best fit is shown in Figure 6.

We find good agreement between our synthetic data of best fit and the MOSES data. Figure 7 compares the mean cross-correlation of the difference image rows from the slightly
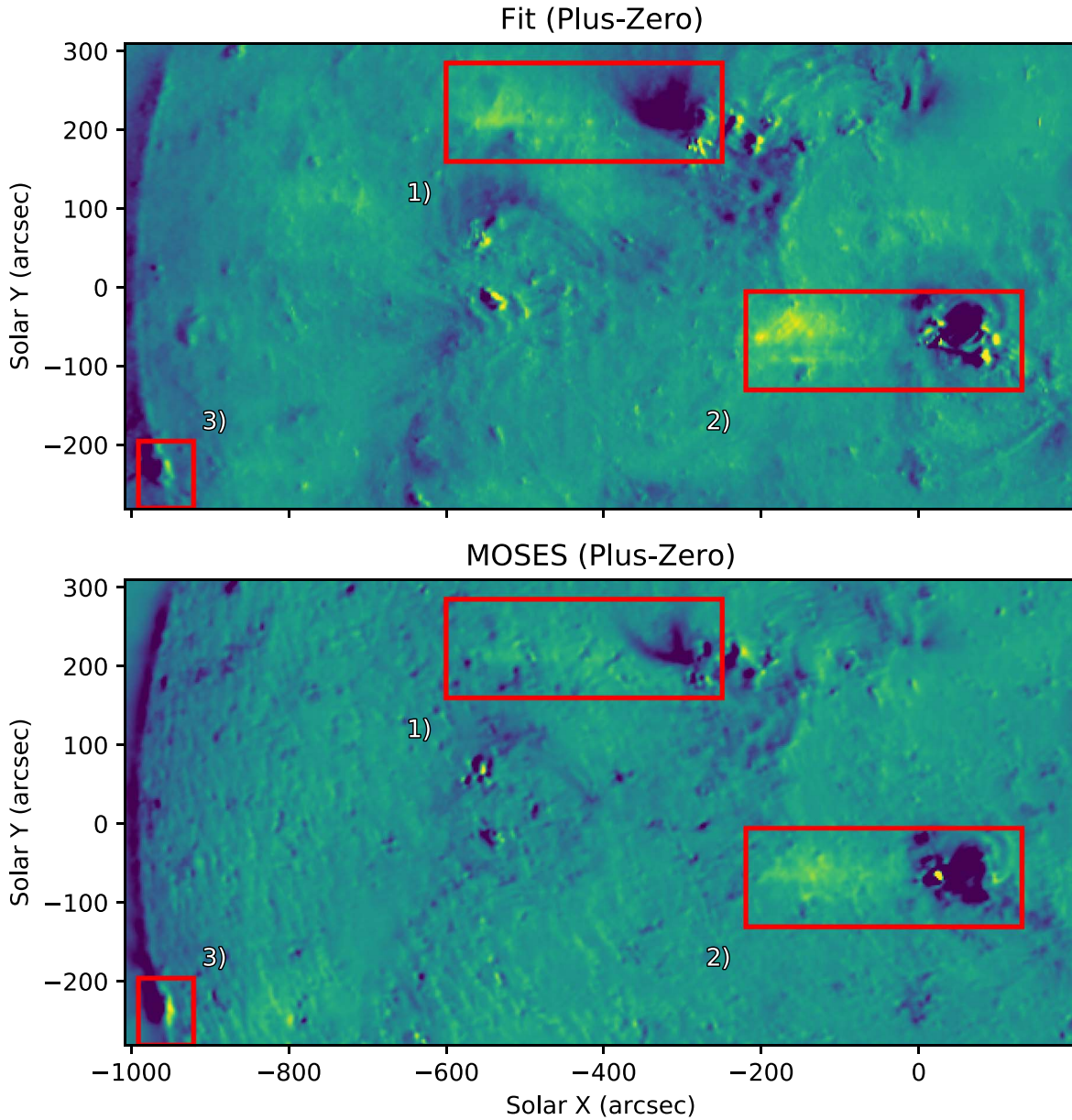
Figure 8. The $I_{+1} - I_0$ difference image, also shown in Figure 1(c), alongside the same difference image prepared from the synthetic MOSES images of best fit. Identical regions 1–3 are boxed in each image for comparison.

blurred MOSES data to the same cross-correlation of the synthetic data. Comparing the two curves shows notable agreement in a few places, including around zero lag and all positive lags. Negative lags match less closely, although the shape between zero and approximately −600 pixels is similar. Considering that we have attempted to use a single DEM to represent the quiet Sun over a very large field of view, we think the agreement is remarkable.

A synthetic difference image of best fit (I'_{+1} minus I'_0) is shown along with the corresponding MOSES difference image in Figure 8. In the synthetic difference image, each feature identified in Figure 1 has been successfully reproduced. The dark imprints of the "wishbone" (region 1) and nearby active region (region 2) are clearly visible and are adjacent to respective lighter smears of intensity to the left of each of them. Region 3, while not as sharp in the synthetic images, is reproduced at the limb with the same close separation between the positive and negative lobes.

Using the DEM of best fit, we also generated an average spectrum for the MOSES data weighted by the instrument's wavelength-dependent throughput (Figure 9). The synthetic spectrum of best fit was generated using the same constant pressure, abundance file, and spectral range as were used in the forward model (Section 3.3). MOSES images are dominated by the He II doublet near 303.7. Si XI 303.3 Å, while much dimmer than He II, has the second-highest intensity and represents approximately 8% of the total intensity. The other notable, and unexpected, contribution to the image intensity is from the host of lines between 310 and 320 angstroms, the brightest being from Mg VIII and Si VIII. Table 1 shows the 25 brightest lines observed by MOSES, their intensity relative to He II 303.78 Å, and their dispersion in pixels and arcsecond, making it easier to assign spectral content to features in the difference images. Table 2 shows the total intensity contribution from each of the brightest ions.
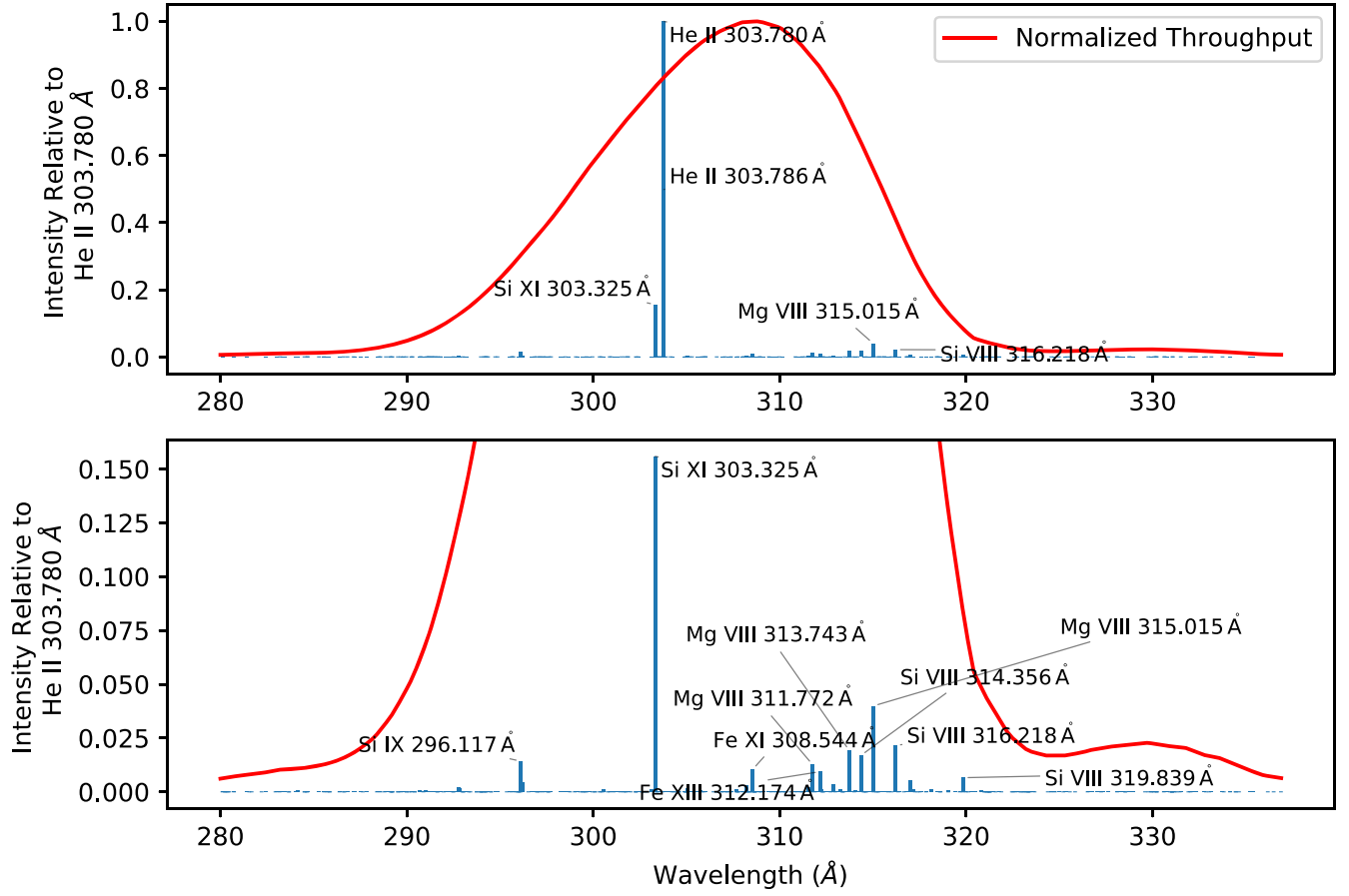
Figure 9. Using the DEM of best fit shown in Figure 6, we generated the above synthetic spectrum using Chianti. Each line intensity has also been weighted by the wavelength-dependent throughput of the MOSES optical system (normalized and shown in red).

Table 1
Pixel Dispersion of Dominant Spectral Lines with Intensities Relative to He II 303.78 Å

Spectral Line	Relative Intensity (%)	Dispersion (pixels)	Dispersion (arcsec)
Si IX 292.80 Å	0.19	−378.62	−227.17
Si IX 296.12 Å	1.42	−264.24	−158.54
Si IX 296.21 Å	0.46	−260.93	−156.56
Si XI 303.32 Å	15.59	−15.69	−9.41
Fe XIII 303.36 Å	0.62	−14.34	−8.61
He II 303.78 Å	100.00	0.00	0.00
He II 303.79 Å	49.91	0.21	0.12
Al IX 305.05 Å	0.18	43.62	26.17
Si VIII 308.19 Å	0.29	152.03	91.22
Fe XI 308.54 Å	1.04	164.28	98.57
Fe XIII 311.55 Å	0.19	267.83	160.70
Mg VIII 311.77 Å	1.26	275.59	165.35
Fe XIII 312.17 Å	0.94	289.45	173.67
Fe XIII 312.87 Å	0.36	313.38	188.03
Mg VIII 313.74 Å	1.91	343.55	206.13
Si VIII 314.36 Å	1.69	364.69	218.81
Mg VIII 315.01 Å	3.99	387.41	232.45
Si VIII 316.22 Å	2.16	428.90	257.34
Mg VIII 317.03 Å	0.53	456.83	274.10
Si VIII 319.84 Å	0.66	553.76	332.26

Table 2
Average MOSES Image Spectral Content

Ion	Contribution
He II	80.55%
Si XI	8.37%
Mg VIII	4.14%
Si VIII	2.65%
Si IX	1.33%
Fe XIII	1.29%
Other	1.67%

5. Discussion and Conclusions

MOSES was successful in its goal of capturing solar images in the He II 303.8 Å emission line. Despite the use of a narrowband multilayer coating on both the primary and secondary optics, MOSES captured several solar features not easily attributed to the dominant He II 303.8 Å or nearby strong Si XI 303.3 Å lines. In order to identify and quantify the spectral content of these additional features, we cross-correlated two MOSES difference images and identified peaks in correlation as significant and indicative of spectral contamination. Using a forward model that combines four cotemporal EIT images with synthetic spectra from Chianti, we created synthetic MOSES difference images with known spectral content that could be cross-correlated and compared to the MOSES difference image cross-correlation function. By

varying the average DEM used, we modified the spectral content of the synthetic MOSES data until we minimized the differences between the synthetic and real cross-correlation functions, the results of which are displayed in Section 4.

Compared to other solar DEMs, like those included in the Chianti software package, our DEM of best fit (Figure 6) shows a huge increase in emission measure between log $T = 4$–5 K. This result is artificial and is caused by a significant lack of modeled intensity in the He II 303.8 Å emission line when using Chianti. The He II 303.8 Å intensity is low by up to an order of magnitude when modeled under classical assumptions, and its lack of emission has been attributed to a host of factors including a lack of ionization equilibrium (Golding et al. 2017). Since the MOSES passband is absent of any other bright, cool lines ($<.1$ MK), our fit can increase the emission measure at low temperatures, resulting in an increase in the intensity of He II 303.8 Å alone, allowing for a more accurate intensity ratio between it and nearby hot emission lines like Si XI 303.3 Å. We find an average line ratio between He II 303.8 Å and Si XI 303.3 Å intensities of $\approx 10{:}1$, which is comparable to ratios measured by other slit spectrographs in regions of moderate solar activity (Cushman & Rense 1978; Brosius et al. 1998, 2000).

It is also important to note that, although we chose to use a DEM as the basis of our fit, we do not consider it to be an accurate average DEM of the Sun across the MOSES field of view. The formation temperatures of lines within the MOSES passband very sparsely cover the range of log $T = 4$–6.5, allowing multiple DEMs to represent the same spectral content. Despite the parameter space being very degenerate, we chose to vary emission measure, rather than individual line intensities, to ensure our final fits have physically realizable line ratios.

The temperature coverage of EIT, used to create the synthetic data, is also very sparse. Luckily, the dominant lines in each of the four included EIT images have peak formation temperatures that closely match the peak formation temperatures of the brightest lines imaged by MOSES. The four EIT channels used, He II 304 Å, Fe IX 171 Å, Fe XII 195 Å, and Fe XV 284 Å, have respective peak formation temperatures of log $T = 4.7$ K, 5.9 K, 6.2 K, and 6.3 K, calculated using Chianti. The bright, hotter lines imaged by MOSES, namely from Mg VIII, Si VIII, and Si XI, have respective peak formation temperatures of log $T = 5.9$ K, 5.95 K, and 6.2 K. This allows for synthetic MOSES data with key intensity contributors well-represented, as is evident when comparing features in the synthetic difference images of best fit to those in the MOSES difference images (Figure 8).

The most mysterious features in the MOSES difference images, those that motivated this study, are regions 1 (the "wishbone") and 2 identified in Figures 1 and 8. These two features are very coronal in appearance and easily identifiable in the hotter EIT channels, but they cannot be attributed to the most obvious source of contamination in any He II image, Si XI 303.3 Å, due to the lack of positive component ≈ 15.7 pixels away like that seen in region 3. The presence of a faint, light smear left of the wishbone indicates that it is from emission at longer wavelengths than He II 303.8 Å, but a lack of clear positive wishbone makes it difficult to attribute it to a single contaminant line. The best-fit spectrum (Figure 9) shows a host of lines between 310 and 320 angstroms, mostly emitted by the Mg VIII and Si VIII ions, the strongest being Mg VIII 315 Å (Also identified by Rust 2017). Despite their individually weak intensity, combined they contribute on the order of the same intensity as Si XI 303.3 Å. Due to spectral dispersion, these lines are very faint in the MOSES outboard order and could likely be neglected. In the zero-order image, all of these faint lines land in the same place on the detector, which is why these features appear so clearly when subtracting the zero order. The intensity contribution from lines other than He II 303.8 Å and Si XI 303.3 Å amounts to around 10% of the total intensity in the zero order and comes from tens of lines that may be easily overlooked during analysis or instrument development. Some of these lines are shifted hundreds of pixels, causing feature within the field of view of the MOSES zero order to be shifted out and those outside to be shifted in the outboard orders. This results in different total intensities existing in each spectral order, which could lead to confusion when comparing orders during inversion.

While overlapping intensity from different spectral lines is inevitable in this type of instrument, the use of a zero-order (undispersed) image and a lack of a clearly defined field of view in MOSES exacerbates the problem of spectral contamination. ESIS (J. D. Parker et al. 2022, in preparation; R. T. Smart et al. 2022, in preparation), our second-generation rocket-borne slitless spectrograph, builds off the MOSES concept and improves on it in several ways. The most relevant improvements include an intermediate focal plane, a field stop that clearly defines the instrument field of view, and four channels rather than three, none of which are undispersed. Including a field stop defines the same field of view for every channel and solves the problem of highly shifted features existing in some orders but not others. Even with a clearly defined field of view, features in the zero-order image would still have intensity from lines that are dispersed off the detector in the outboard orders. The ambiguity of spectral content makes it difficult to compare its intensity to outboard orders without DEM forward modeling. Using all dispersed orders, as is done in ESIS, makes it much easier to compare the intensity of solar features from specific emission lines, and tends to reduce the effect of contaminant lines on measured intensity by dispersing them across the image. We think this approach will prove particularly advantageous with a high-dispersion instrument whose chief science objective is to resolve the profiles of strong lines. The considerations are rather different when the instrument is designed from the start to reconstruct DEMs, as with COSIE (Winebarger et al. 2019) or the recently selected MOXSI (Caspi et al. 2021), both of which use undispersed images. These instruments have much larger spectral ranges than MOSES and therefore are better suited to constraining a DEM in every pixel when inverting. That being said, those inversions rely heavily on assumptions baked into atomic physics codes (abundance and density choices, the assumption of ionization equilibrium, etc.) and precise knowledge of the differences in effective area as a function of wavelength between channels, as does the analysis in this paper. If an inversion with zero assumptions is preferred, then having different dispersed images with the same spectral content, effective area, and field of view is preferred.

In the MOSES design, the zero order was intended to improve the spatial resolution, which is otherwise blurred by the line profiles, in the horizontal direction. It served very effectively in this role. With ESIS, we oriented the dispersion of its four channels in four different directions. Each ESIS channel has its highest resolution in the direction perpendicular to the dispersion, and together they are able to separate closely spaced features with any orientation. As our inversion skill improves, we will learn whether this approach to high-resolution imaging is as successful as the zero order.

In summary, we have developed a forward model of the MOSES instrument that combines the Chianti database and images from EIT to form synthetic MOSES data with known spectral content. Our fits match the MOSES data well and indicate that the unexpected solar features identified in MOSES difference images are composed of tens of dim lines that, in the aggregate, contribute approximately 10% of the average intensity in the zero-order image and are smeared over many hundreds of pixels in the outboard orders. This unexpected spectral content makes it difficult to compare the intensity of certain features between spectral orders, and if not properly accounted for, could lead to poor convergence when inverting slitless spectrograph data. Our analysis has led us to comment on the advantages and disadvantages of zero-order imaging in a slitless spectrograph. These considerations should aid in the design of future instruments of this type, and serve as a reminder to carefully consider the spectral content of undispersed channels when interpreting the data.

ORCID iDs

Jacob D. Parker ⬤ https://orcid.org/0000-0001-8732-8284
Charles C. Kankelborg ⬤ https://orcid.org/0000-0002-1992-7469

References

Athiray, P. S., Winebarger, A. R., Barnes, W. T., et al. 2019, ApJ, 884, 24
Brosius, J. W., Davila, J. M., & Thomas, R. J. 1998, ApJS, 119, 255
Brosius, J. W., Thomas, R. J., Davila, J. M., & Landi, E. 2000, ApJ, 543, 1016
Caspi, A., Shih, A. Y., Panchapakesan, S., et al. 2021, AAS Meeting Abstracts, 53, 216.09
Cook, J. W., Newmark, J. S., & Moses, J. D. 1999, in ESA Special Publication, 8th SOHO Workshop: Plasma Dynamics and Diagnostics in the Solar Transition Region and Corona, Vol. 446, ed. J. C. Vial & B. Kaldeich-Schü (The Netherlands: ESA), 241
Courrier, H. T., & Kankelborg, C. C. 2018, JATIS, 4, 018001
Culhane, J. L., Harra, L. K., James, A. M., et al. 2007, SoPh, 243, 19
Cushman, G. W., & Rense, W. A. 1978, SoPh, 58, 299
Del Zanna, G., & Young, P. R. 2020, Atoms, 8, 46
Delaboudinière, J. P., Artzner, G. E., Brunaud, J., et al. 1995, SoPh, 162, 291
Dere, K. P., Landi, E., Mason, H. E., Monsignori Fossi, B. C., & Young, P. R. 1997, A&AS, 125, 149
Feldman, U. 1992, PhyS, 46, 202
Fox, J. L. 2011, PhD thesis, Montana State Univ.
Fox, J. L., Kankelborg, C. C., & Thomas, R. J. 2010, ApJ, 719, 1132
Golding, T. P., Leenaarts, J., & Carlsson, M. 2017, A&A, 597, A102
Golub, L., Cheimets, P., DeLuca, E. E., et al. 2020, JSWSC, 10, 37
Harra, L., Matthews, S., Long, D., et al. 2020, SoPh, 295, 34
Harra, L. K., Hara, H., Doschek, G. A., et al. 2017, ApJ, 842, 58
Kosugi, T., Matsuzaki, K., Sakao, T., et al. 2007, SoPh, 243, 3
Owens, S. M., Gum, J. S., Tarrio, C., et al. 2005, Proc. SPIE, 5900, 5
Rust, T., & Kankelborg, C. C. 2019, ApJ, 877, 59
Rust, T. L. 2017, PhD thesis, Montana State Univ.
Tousey, R., Bartoe, J. D. F., Bohlin, J. D., et al. 1973, SoPh, 33, 265
Winebarger, A. R., Weber, M., Bethge, C., et al. 2019, ApJ, 882, 12
Zhitnik, I. A., Kuzin, S. V., Oraevskii, V. N., et al. 1998, AstL, 24, 819